Quadratic-Attraction Subdivision with Contraction-Ratio $\lambda = \frac{1}{2}$

Kęstutis Karčiauskas[a], Jörg Peters[b,*]

[a] *Institute of Mathematics, Vilnius University, Lithuania*
[b] *Department CISE, University of Florida, USA*

Abstract

Classic generalized subdivision, such as Catmull-Clark subdivision, as well as recent subdivision algorithms for high-quality surfaces, rely on slower convergence towards extraordinary points for mesh nodes surrounded by $n > 4$ quadrilaterals. Slow convergence corresponds to a contraction-ratio of $\lambda > 0.5$. To improve shape, prevent parameterization discordant with surface growth, or to improve convergence in isogeometric analysis near extraordinary points, a number of algorithms explicitly adjust λ by altering refinement rules. However, such tuning of λ has so far led to poorer surface quality, visible as uneven distribution or oscillation of highlight lines. The recent Quadratic-Attraction Subdivision (QAS) generates high-quality, bounded curvature surfaces based on a careful choice of quadratic expansion at the central point and, just like Catmull-Clark subdivision, creates the control points of the next subdivision ring by matrix multiplication. Unfortunately, QAS shares the contraction-ratio $\lambda_{CC} > 1/2$ of Catmull-Clark subdivision when $n > 4$. This shortcoming is finally remedied by the presented improvement QAS$_+$ of QAS. For $n = 5, \ldots, 10$, the convergence is made a uniform $\lambda = \frac{1}{2}$ as in tensor-product case and without sacrificing surface quality.

1. Introduction

Classical subdivision algorithms, and Catmull-Clark subdivision [1] in particular, generalize uniform B-spline or box-spline refinement [2, Ch 7]. Notably, for tensor-product B-splines uniform refinement splits each parameter interval into two equal parts by knot insertion, say by the Oslo algorithm [3], yielding tensor-product B-spline subdivision with contraction-ratio $\lambda = 1/2$. By contrast, currently available generalized subdivision to mesh nodes surrounded by $n > 4$ quadrilaterals (an extraordinary point, (*eop*)) either feature slower convergence $\lambda \in (\frac{1}{2}..1)$ or yield poor surface quality, visible as an uneven distribution or oscillation of highlight lines. Slow convergence distorts the parameterization near extraordinary points compared to regular tensor-product neighborhoods: the parameter range splits in a binary fashion, but the surface grows less than half-ways towards its limit extraordinary point [4]. Moreover, $\lambda > 0.5$ implies slower error reduction when computing functions on surfaces, say as solutions to partial differential equations.

The new Quadratic-Attraction Subdivision (QAS_+) with $\lambda = \frac{1}{2}$ finally resolves the shape vs. speed trade off by combining good shape with uniform convergence near the extraordinary point. QAS$_+$ is an improvement of the recent algorithm [5]. We summarize the contributions.

- Explicit formulas for an implementation of QAS$_+$ as matrix multiplication to generate nested surface rings.
- The resulting uniform highlight line distribution indicate high-quality surfaces.
- The surfaces are curvature-bounded at extraordinary points and C^2 everywhere else.

*Corresponding author:
Email address: jorg.peters@gmail.com (Jörg Peters)

- The improved QAS$_+$ algorithm has $\lambda = \frac{1}{2}$ everywhere.
- The surfaces can be chosen either of degree bi-4 (bi-quartic) or, at the cost of more pieces, of degree bi-3.
- A new technical approach: QAS$_+$ bakes in the contraction speed $\lambda = \frac{1}{2}$ by constructing a special characteristic bi-4 C^2 map.
- The approach renders the analysis of the limit properties simple.
- QAS$_+$ is more flexible than QAS by allowing the quadratic expansion $\mathbf{q}$ to be C^0, apart from a well-defined tangent plane at the extraordinary point.

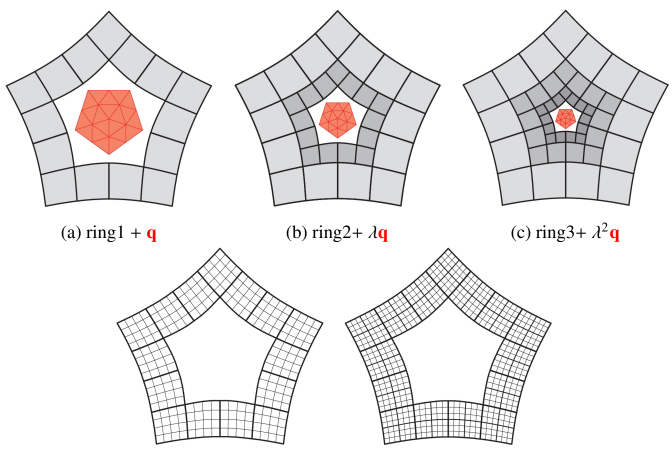

(a) ring1 + $\mathbf{q}$ (b) ring2+ $\lambda\mathbf{q}$ (c) ring3+ $\lambda^2\mathbf{q}$

(d) $3n$ bi-4 (e) $12n$ bi-3

Figure 1: Two new flavors of QAS: QAS$^4_+$ of degree bi-4 and QAS$^3_+$ of degree bi-3. (a,b,c) share the connectivity of control nets and refined quadratic expansions (generated from the input of Fig. 2(b,c)) but QAS$^4_+$ and QAS$^3_+$ generate different contracting surface rings whose Bernstein-Bézier coefficient nets (BB-nets) are shown in (d) $3n$ bi-4 patches and (e) $12n$ bi-3 pieces viewed as $3n$ 2× macro-patches.

1.1. *Literature: classical, guided and augmented subdivision*

There is a rich choice of surface constructions, ranging from rational blending constructions [6, 7], to manifold splines [8], geometrically continuous surfaces [9, 10, 11, 12] singular [13, 14] and rational singular [15] constructions and even curved knotline splines [16]. A recent survey, [17] provides both an overview and a classification. Here we focus on a class of singular surface parameterizations known as subdivision surfaces. Due to their intuitive simplicity as local mesh refinement while generalizing B-splines, subdivision algorithms are widely used in shape modelling. Near extraordinary points, [18] showed that subdivision can be expressed and (partly) analyzed as multiplication with a sparse matrix (see also [19]). Various optimizations strategies, called 'tuning', and based on rules with a larger footprint have been proposed to address shape problems, such as pinching of highlight lines of the dominant Catmull-Clark subdivision [1] near the extraordinary point, and to achieve bounded curvature. However such local tuning typically results in oscillating curvature, and negatively affects the visual quality in the vicinity of the extraordinary point, or generates noticeable artifacts in the transition from the regular surrounding surface, see e.g. [20] which summarizes [21, 22]. In particular, moving the subdominant eigenvalue λ close to $\frac{1}{2}$ or even to 0.4 in order to improve the convergence rate for isogeometric analysis, [21, 22] sacrifice shape good shape in the larger neighborhood of the extraordinary point, and are not of bounded curvature for $n > 7$. Generalizing Catmull-Clark subdivision for irregular knot spacings, [23] and [24] present a similar loss in highlight line uniformity when λ is decreased.

Guided Subdivision harnesses a larger number of degrees of freedom than most tuned approaches by first computing a fixed surface prototype, called the guide surface, from a control net. Each refinement step adds a surface ring into a nested sequence whose limit converges to the guide. While the shape is typically very good, the separate construction of the guide makes this approach more complex than standard subdivision. In response, starting with Point-Augmented Subdivision (PAS) [25], newer algorithms combine the superior shape of guided subdivision with the simplicity of classical subdivision. The augmented subdivision steps are formulated, just as classical subdivision algorithms, as matrix multiplication. This simplifies implementation, and public code is available, e.g. [26]. PAS surfaces exhibit considerably better curvature distribution than optimized classical algorithms, both in-the-large and in the vicinity of the extraordinary point. However, PAS algorithms are not curvature bounded. This shortcoming was remedied by Quadratic-Attraction Subdivision [5] (QAS) by prescribing a central quadratic expansion. The approach leverages the key advantage of guided over conventional subdivision: decoupling shape finding from enforcing smoothness and curvature properties in vicinity of extraordinary point. QAS refinement can be implemented as matrix multiplication. The QAS curvature is bounded at extraordinary point and the shape quality is good both in vicinity of extraordinary point and in-the-large. Since a rigorous measure of surface quality remains illusive, and since highlight lines and curvature distribution are the established analysis tools in industrial shape design, we declare *shape good*, if, empirically and unless wanted as part of the design intent, the surfaces have uniform highlight lines and non-oscillating curvature.

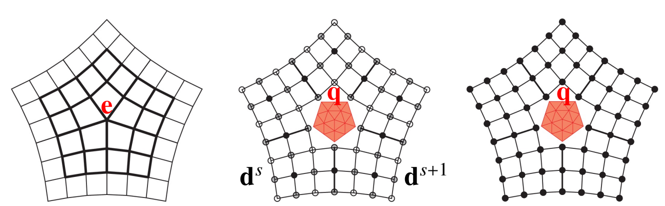

(a) $\mathbf{c}$-net (b) bi-4 $\mathbf{d}$-net + $\mathbf{q}$ (c) bi-3 $\mathbf{d}$-net + $\mathbf{q}$

Figure 2: Control nets. (a) $\mathbf{c}$-net (**thick lines**) with irregular node $\mathbf{e}$ for Catmull-Clark subdivision (CC), extended by one surrounding quad ring. While the $\mathbf{c}$-net suffices to define QAS$_+$, the surrounding quads are needed by the latest tuned subdivision methods that we compare to, and serve to gauge the transition to a regular C^2 tensor-product spline surface. (b) A $\mathbf{d}$-net with $12n$ nodes. Different node fill (black, gray, white) indicates different knot multiplicity. The quadratic $\mathbf{q}$, defined by bi-4 QAS^4 of [5]. (c) $12n$ node $\mathbf{d}$-net and quadratic $\mathbf{q}$ that define QAS^3 of [5].

2. Framework of improved QAS_+ quadratic-attraction subdivision

Before diving into the technical details, we provide a step by step overview of the approach:

1 Transform the input **c**-net (**thick lines** in Fig. 2a) into a **d**-net, Fig. 2b exactly as for bi-4 quadratic-attraction subdivision (QAS), or, alternatively bi-3 QAS, Fig. 2c.

2 Initialize the quadratic expansion $\mathbf{q}$, central in Fig. 2b,c.

3 Special QAS^4_+ rules for $n > 4$ define the innermost $6n$ nodes of the refined net (magenta nodes in Fig. 3; the remaining $24n$ black nodes stem from uniform refinement of C^2 bi-4 splines).

4 The entire refined net in Fig. 3 is converted to the ring of $3n$ C^2-connected bi-4 patches displayed in Fig. 1d.

5 Iterate, see Fig. 1(a,b,c): Restriction of $\mathbf{q}$ over a scaled subdomain defines the new quadratic expansion $\tilde{\mathbf{q}}$. Steps 3,4 produce another bi-4 ring C^2-connected to its predecessor.

For $n = 3$, the subdominant eigenvalue λ of QAS is less than $1/2$ and the shape is very good. So there is no need to derive new QAS_+ formulas for $n = 3$ (that would slow down convergence).

While bi-3 patchworks, i.e. conventional bi-3 subdivision, is more popular than bi-4 counterparts, bi-4 QAS^4_+ takes the lead, because the derivation of bi-4 refinement rules is considerably easier than for the split bi-3 alternative. Section 6 exhibits a simple symbolic procedure that transforms the refinement rules of QAS^4_+ to those of QAS^3_+, and one QAS^3_+ step produces $12n$ bi-3 patches that can be viewed as $3n$ 2×2 macro-patches, see Fig. 1e. That is, a layout of QAS^3_+ is the same as for the curvature-bounded subdivision in the literature.

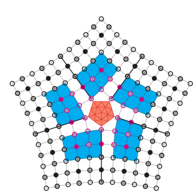

Figure 3: Once-refined QAS^4_+ net; cf. Fig. 2b.

2.1. Technical Tools

To emphasize that the tools of this section are known and already well-expressed, for completeness we closely replicate the following techniques from [5], with permission of the authors. It is convenient to represent subdivision surface rings by tensor-product patches in Bernstein-Bézier form (BB-form, [27, 28]) of bi-degree d (bi-d):

$$\mathbf{p}(u, v) := \sum_{i=0}^{d} \sum_{j=0}^{d} \mathbf{p}_{ij} B^d_i(u) B^d_j(v), \quad 0 \le u, v \le 1,$$

where $B^d_k(t) := \binom{d}{k}(1-t)^{d-k}t^k$ Bernstein polynomials. As usual, the *BB-coefficients* $\mathbf{p}_{ij} \in \mathbb{R}^3$ are connected to $\mathbf{p}_{i+1,j}$ and $\mathbf{p}_{i,j+1}$ wherever possible to form the *BB-net*.

The coordinate-wise order 3 Taylor expansion of a map f at a corner of the unit square can be expressed as a 3×3 BB-net (right of $\sim$ in Fig. 4) of degree bi-d. Three such *corner jets*

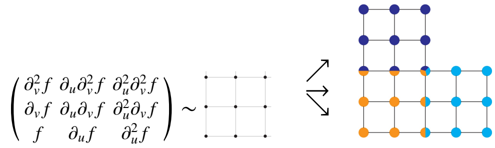

Figure 4: Three corner jets (rotated by $\pi/2$ for • and $-\pi/2$ for • so that the corner BB-coefficient is f evaluated at the corresponding corner of the unit square) assembled into an L-net of degree bi-4.

(cyan, orange and blue) of degree bi-4 can be merged into an L-net by averaging the BB-coefficients at overlapping locations, see Fig. 4, right. The expansion across a boundary is called a *tensor-border* (and is called 'ribbon' in other publications). A bijection, whose formulas are given in [5, Sect 3], between the control nets of bi-4 and bi-3 tensor-borders (of QAS^4 and QAS^3) is illustrated in Fig. 5:

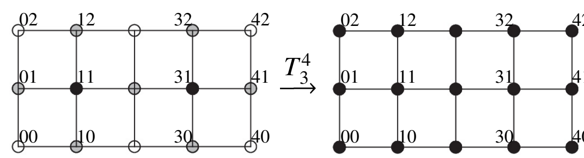

(a) **d** of QAS^4 (b) **d** of QAS^3

Figure 5: The bijective transformation T^4_3 from a bi-4 to a bi-3 tensor-border.

Another bijection is the change of bases from B-spline to BB-form, called *B-to-BB conversion*. See [29, Eq. 6] for B-to-BB conversion of bi-4 C^2 splines.

3. The bi-4 characteristic map χ

A carefully constructed C^2 bi-4 characteristic map χ with a scaling factor $\lambda = \frac{1}{2}$ is the technical achievement at the core of QAS_+. Characteristic maps are usually determined by the subdivision rules, as eigenfunctions of the subdominant eigenvalue λ. By contrast, here χ *governs* the refinement rules – and the calculation of eigenspectrum and eigenfunctions become a confirmation of expected properties. Since well-behaved characteristic maps can also be used for other subdivision and finite polynomial constructions, we describe χ in detail. The characteristic map of QAS^4_+ is visually identical to χ but uses truncated numbers, see Section 4.

As for Catmull-Clark subdivision, χ is rotationally symmetric and symmetric with respect to the sector bisectrix (the bisectrix is the x-axis in the illustration Fig. 6a). This imposes the Ansatz

$$\begin{aligned}
&\bar\chi_{40} := (\hat{\mathsf{c}}, \hat{\mathsf{s}}),\ \bar\chi_{41} := (z_0\hat{\mathsf{c}}, z_0\hat{\mathsf{s}}),\ \bar\chi_{42} := (z_1\hat{\mathsf{c}}, z_1\hat{\mathsf{s}}),\\
&\bar\chi_{00} := (z_2, 0),\ \bar\chi_{11} := (z_3, 0),\ \bar\chi_{22} := (z_4, 0),\\
&\bar\chi_{10} := (z_5, z_6),\ \bar\chi_{20} := (z_7, z_8),\ \bar\chi_{21} := (z_9, z_{10}),\\
&\alpha := \frac{2\pi}{n}, \mathsf{c} := \cos\alpha, \mathsf{s} := \sin\alpha, \hat{\mathsf{c}} := \cos\frac{\alpha}{2}, \hat{\mathsf{s}} := \sin\frac{\alpha}{2}.
\end{aligned} \tag{1}$$

The remaining BB-coefficients $\bar\chi_{3j} \in \mathbb{R}^2$, $j = 0, 1, 2$, of the *tensor-border* $\bar\chi$ of χ are defined by requirement that the adjacent sectors of $\bar\chi$ be C^2-connected.

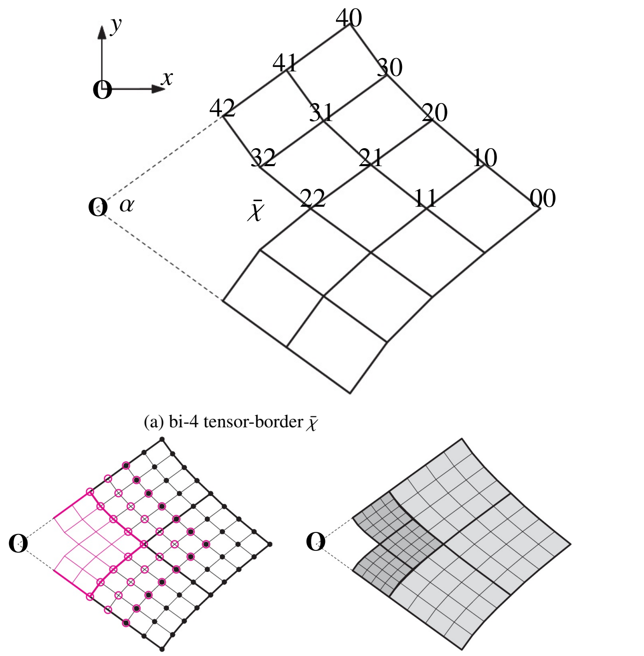

(a) bi-4 tensor-border $\bar{\chi}$

(b) split, scale. merge

(c) $\chi + \frac{1}{2}\chi$

Figure 6: (a) Structure and labeling of $\bar{\chi}$. (b) Uniform split (the •s) of $\bar{\chi}$ and scaled $\frac{1}{2}\chi$ (edges) followed by C^2 extension (∘), backwards. (c) C^2 connected light gray χ and darker gray $\frac{1}{2}\chi$.

Next, $\bar{\chi}$ is evenly split into two pieces along the boundary segments, see the •s in Fig. 6b. Then $\bar{\chi}$ is scaled with respect to the origin **O** by $\frac{1}{2}$ (in Fig. 6b $\frac{1}{2}\bar{\chi}$ is the magenta quadrant at **O**). Joining the scaled copy C^2 with the split outer copy, defines the BB-coefficients marked ∘ and requires the overlapping BB-coefficients (marked by both ∘ and •) to match. This is enforced by solving a system of linear equations with respect to the free scalars z_i, $i = 0, \dots, 10$ and determines z_0, z_5, z_i, $i = 7, \dots, 10$ in terms of the remaing scalars z_1, z_2, z_3, z_4, z_6. To set the unconstrained z_1, z_2, z_3, z_4, z_6, we compared minimization of the functional $\mathcal{F}_k f := \int_0^1 \int_0^1 \sum_{i+j=k,i,j\geq 0} \frac{k!}{i!j!} (\partial_s^i \partial_t^j f(s,t))^2 \, ds \, dt$ for $k = 2, \dots, 7$ over the 3 bi-4 patches of one sector. For all k, the distributions of BB-coefficients looks visually acceptable. The most uniform distribution is obtained when $k = 4$. For all k, z_1 is very close to $\frac{1}{2}$ and z_2 is very close to $\sqrt{2}$. Therefore we set: $z_1 := \frac{1}{2}$ (implying $z_0 := \frac{3}{4}$) and $z_2 := \sqrt{2}$ which implies for $i = 5, 7, \dots, 10$

$$
\begin{aligned}
z_i &:= \frac{1}{k_i}(v_2^i z_2 + v_3^i z_3 + v_4^i z_4 + v_6^i z_6 + \dot{v}^i), \\
k_5 &:= 4\bar{k},\ k_7 := 2\bar{k},\ k_8 := \bar{k},\ k_9 := 4\bar{k},\ k_{10} := \bar{k}, \\
\bar{k} &:= 123199 + 64716\mathrm{c}
\end{aligned}
\tag{2}
$$

where the scalars v_j^i, $\dot{v}_j^i$ are listed in Appendix A. The functional $\mathcal{F}_4$ need now only be minimized with respect to z_3, z_4, z_6. Appendix B lists their values for valencies $n = 5, \dots, 10$ with 10 digits after the decimal point.

In summary, scaling χ by $\frac{1}{2}$ yields a sequence of C^2 rings that are C^2 joined. Fig. 6c displays one sector each, of two consecutive rings.

We note that the choice $z_0 := \frac{3}{4}$, $z_1 := \frac{1}{2}$ and $z_2 := \sqrt{2}$ matches the exact values for the regular case of valence $n = 4$, but that nevertheless, derivation by analogy fails. For example, setting z_6 so that the $\bar{\chi}$ edges (30, 31), (31, 32), (20, 21), (21, 22) become parallel to the sector separating line **O**, and the resulting $\bar{\chi}_{40}$ yields decidedly worse quality than our default choice based on optimizing $\mathcal{F}_4$. We also caution that, while different choices of k for the functional lead to visually almost identical bi-4 χ and similar-looking rings, quality deteriorates with iteration for $k \neq 4$.

Fig. 7 juxtaposes the tensor-border $\bar{\chi}$ and its sibling, the tensor-border $\bar{\chi}^{CC}$ of the characteristic map of Catmull-Clark subdivision. For better comparison the $\bar{\chi}^{CC}$ is degree-raised to bi-4 and normalized so that $\bar{\chi}_{40}^{CC} = \bar{\chi}_{40}$. We observe that $\bar{\chi}$

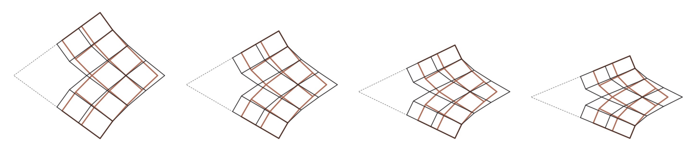

(a) $n = 5$ (b) $n = 6$ (c) $n = 7$ (d) $n = 8$

Figure 7: Black bi-4 characteristic tensor-border $\bar{\chi}$ and brown characteristic tensor-border $\bar{\chi}^{CC}$ of Catmull-Clark subdivision degree-raised to bi-4 for valencies $n = 5, 6, 7, 8$.

is more pointed and covers larger area than degree-raised $\bar{\chi}^{CC}$, due to the geometry of faster contraction.

4. QAS$^4_+$: improved Quadratic-Attraction Subdivision of degree bi-4

Here we focus on the new aspects that distinguish QAS$^4_+$ from its ancestor QAS^4. For completeness, we explain technical details akin to QAS in Appendix D.

4.1. Overview: structure and refinement of the bi-4 d-net

The input of QAS$^4_+$ are a **d**-net and a quadratic expansion **q**, see Fig. 9a. Since the surface rings are of degree bi-4 and the smoothness is C^2, the corresponding B-spline representation has alternating double and single knots in each of the parameter directions. In Fig. 9a nodes corresponding to double knots in both parameters are marked •, single are marked the ∘ and control nodes corresponding to a single knots in one and a double in the other are circled •.

Fig. 9b shows the $6n$ magenta control points generated by the new refinement rules. Combined with those obtained by uniform B-spline refinement rules, one refinement step produces $30n$ new nodes.

4.2. Choice and initialization of the quadratic expansion q at the extraordinary point

The quadratic expansion at the eop defines $f(\mathbf{p})$, $\partial_u(\mathbf{p})$, $\partial_v(\mathbf{p})$, $\partial_{uu}(\mathbf{p})$, $\partial_{uv}(\mathbf{p})$, $\partial_{vv}(\mathbf{p})$. A C^2 limit surface requires that all sectors share the same expansion (using the labels of Fig. 29e), i.e.

$$
\begin{pmatrix} \mathbf{q}_1^{s+1} \\ \mathbf{q}_2^{s+1} \\ \mathbf{q}_3^{s+1} \\ \mathbf{q}_4^{s+1} \\ \mathbf{q}_5^{s+1} \\ \mathbf{q}_6^{s+1} \end{pmatrix} := A \begin{pmatrix} \mathbf{q}_1^{s} \\ \mathbf{q}_2^{s} \\ \mathbf{q}_3^{s} \\ \mathbf{q}_4^{s} \\ \mathbf{q}_5^{s} \\ \mathbf{q}_6^{s} \end{pmatrix}, \quad A := \begin{pmatrix} 1 & 0 & 0 & 0 & 0 & 0 \\ 0 & 0 & 0 & 1 & 0 & 0 \\ 0 & 0 & 0 & 0 & 0 & 1 \\ 2(1-\mathrm{c}) & -1 & 0 & 2\mathrm{c} & 0 & 0 \\ 0 & 0 & 0 & 2(1-\mathrm{c}) & -1 & 2\mathrm{c} \\ 4(1-\mathrm{c})^2 & 4(\mathrm{c}-1) & 1 & 8\mathrm{c}(1-\mathrm{c}) & -4\mathrm{c} & 4\mathrm{c}^2 \end{pmatrix}. \tag{3}
$$

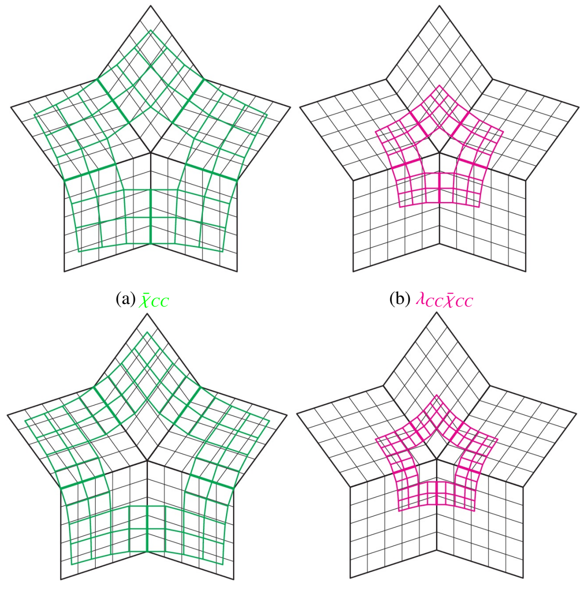

(a) $\bar{\chi}_{CC}$ (b) $\lambda_{CC}\bar{\chi}_{CC}$

(c) $\bar{\chi}$ (d) $\frac{1}{2}\bar{\chi}$

Figure 8: Comparison (a,c) of the green BB-nets of the characteristic tensor-borders $\bar{\chi}^{CC}$ and $\bar{\chi}$. (b,d) scaled tensor-borders, in magenta.

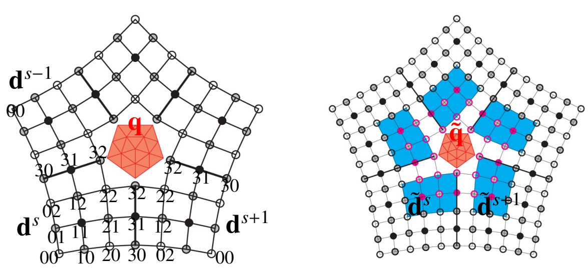

(a) QAS^4_+: $\mathbf{d}$-net + $\mathbf{q}$ (b) QAS^4_+ refinement

Figure 9: QAS^4_+: (a) Bi-4 $\mathbf{d}$-net labels. (b) The nodes marked as •, ∘ and the circled • are obtained from the $\mathbf{d}$-net by regular C^2 bi-4 refinement; new refinement rules define the 6 magenta nodes per sector; the $12n$ cyan-underlaid nodes, $\tilde{\mathbf{d}}^s$, $s = 0, \ldots, n-1$, represent the refined $\mathbf{d}$-net for the next refinement step.

(yielding a 3-fold subsubdominant eigenvalue λ^2). Another novel aspect of QAS^4_+ is the relaxation of the smoothness of $\mathbf{q}$. QAS^4_+ retains curvature-boundedness at extraordinary point even if $\mathbf{q}$ is C^1 or, parts only C^0. This provides wider choice of shape and reproduction near the extraordinary point, with the quadratic-attraction approach maintaining the high quality of resulting surfaces.

Here is a list of three choices for $\mathbf{q}$, , see Fig. 10:

- *C^2 quadratic* $\mathbf{q}$
  The constraints (3) for the sectors of $\mathbf{q}$ to be C^2-connected imply that a quadratic expansion is fully defined by 6 BB-coefficients of one sector, as marked as •, ∘, ∘ in Fig. 10a.

- *C^1 quadratic* $\mathbf{q}$
  To obtain C^1-connected sectors, the last constraint in (3) is replaced by $\mathbf{q}^s_3 := \frac{1}{2\mathrm{c}}(\mathbf{q}^s_5 + \mathbf{q}^{s+1}_5 - 2(1-\mathrm{c})\mathbf{q}^s_4)$. This leaves free for design or computation, an additional n coefficients (marked ∘ in Fig. 10b).

- *C^1-C^0 quadratic* $\mathbf{q}$

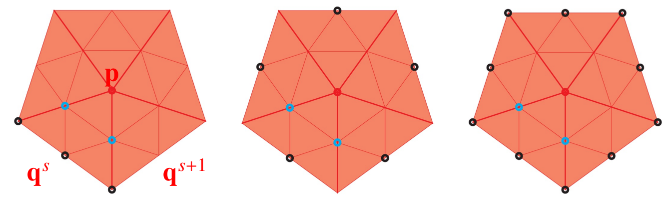

(a) C^2 (b) C^1 (c) C^1-C^0

Figure 10: Three types of quadratic expansion $\mathbf{p}$ at the extraordinary point (eop) : the $\mathbf{p}$ is a central point of $\mathbf{q}$, i.e. $\mathbf{p}{:=}\mathbf{q}^s_1$, $s = 0, \ldots, n-1$. The •, ∘ and ∘ mark the unconstrained BB-coefficients; the • and ∘ define a tangent plane at $\mathbf{p}$. (the labeling of the sectors $\mathbf{q}^s$ and of their entries is the same as in Fig. 29e).

Only the constraints ensuring a well-defined tangent plane at $\mathbf{p}$ remain in (3). The sectors are only C^0-connected, leaving as free $2n$ coefficients (marked ∘ in Fig. 10c).

A careful initialization of $\mathbf{q}$ is crucial for the quality of the resulting surfaces. Fortunately, the C^2 initialization of $\mathbf{q}$ in [5] is a good starting point to perturb coefficients for design intent or computational application: The increased number of degrees of freedom near the extraordinary point, stemming from the C^1 or the C^1-C^0 $\mathbf{q}$, provides good handles for the direct modification of surfaces and for computation on those surfaces.

4.3. Surface ring construction

Appendix C provides explicit formulas of the special refinement rules of the innermost sub-net $\tilde{\mathbf{d}}^s_{ij}$, $i = 1, 2, 3$, $j = 1, 2$ (see magenta nodes in Fig. 9b) in terms of $\mathbf{d}$, $\mathbf{q}$ and $\mathbf{p}$. Fig. 11a groups the so-obtained 45 refined nodes as three 5×5 sub-arrangements, delineated by red, green and blue loops. Applying B-to-BB conversion to each, one at a time, yields three bi-4 patches that form one sector of a new ring, as illustrated in Fig. 11b.

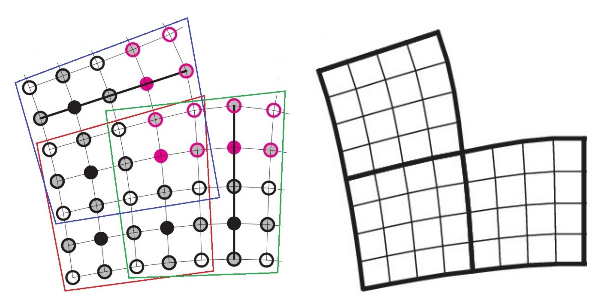

(a) 45 refined nodes (b) 3 bi-4 sector patches

Figure 11: (a) An arrangement of 45 refined nodes for B-to-BB conversion to (b) three bi-4 patches of one sector.

We can now summarize the QAS^4_+ algorithm. The $\mathbf{d}$-net is either directly created by the designer or derived from a Catmull-Clark net according to [29, Fig. 5]. With $\mathbf{p}$ either given or set by [29, Eq. 4], the central $\mathbf{q}$ can be directly designed or obtained algorithmically by [5, (S1–S3)]. Then the algorithm consists of repeated application of the

QAS^4_+ Iteration Step: Refine $\mathbf{d}$-net to $\tilde{\mathbf{d}}$, see Fig. 9 or Fig. 11, the center quadratic and generate a surface ring.

1. Compute $24n$ nodes marked •, ∘ and • by uniform subdivision (knot doubling in each variable) of the bi-4 C^2 spline in B-spline form.
2. Compute $6n$ nodes • by (6) and (7) of Appendix C.
3. B-to-BB convert the $30n$ refined nodes to $3n$ bi-4 patches forming a new surface ring as in Fig. 1c.
4. Define $\tilde{\mathbf{q}}$ from $\mathbf{q}$ by formula (8) of Appendix D.
5. Update $\tilde{\mathbf{q}} \to \mathbf{q}$ and $\tilde{\mathbf{d}} \to \mathbf{d}$.

In Appendix C and D, we truncate the weights involved into refinement rules to 5 decimals since this yields a compact form and does not affect the surface quality. The truncated rules are the 'official' QAS^4_+ rules and provide the following limit analysis.

5. Subdivision limit analysis

For each choice of $\mathbf{q}$, the subdivision matrix M splits into four submatrices, see Fig. 12. One submatrix has only zero entries, and $M_{\mathbf{d}} \in \mathbb{R}^{12n\times 12n}$ does not depend on $\mathbf{q}$.

For the C^2 choice of $\mathbf{q}$ $M_{\mathbf{q}} = S$ of (8). That is $M_{\mathbf{q}}$ displayed in Fig. 12a has eigenvalues 1, λ (2-fold), λ^2 (3-fold).

For a C^1 quadratic $\mathbf{q}$, see Fig. 12b, the free entries are ordered as

$$\mathbf{p}, \mathbf{q}^0_1, \mathbf{q}^0_4, \mathbf{q}^0_5, \mathbf{q}^1_5, \ldots, \mathbf{q}^{n-1}_5,$$

and the submatrix $M_{\mathbf{q}}$ is zero above the main diagonal

$$1, \lambda, \lambda, \overbrace{\lambda^2, \ldots, \lambda^2}^{n \text{ times}} .$$

Therefore the eigenvalues of $M\mathbf{q}$ are 1, 2-fold λ, n-fold λ^2.

For a C^1-C^0 quadratic $\mathbf{q}$, see Fig. 12c, with free entries ordered as

$$\mathbf{p}, \mathbf{q}^0_1, \mathbf{q}^0_4, \mathbf{q}^0_3, \mathbf{q}^0_5, \mathbf{q}^1_3, \mathbf{q}^1_5, \ldots, \mathbf{q}^{n-1}_3, \mathbf{q}^{n-1}_5,$$

the submatrix $M_{\mathbf{q}}$ above main diagonal has only zero entries and the main diagonal is

$$1, \lambda, \lambda, \overbrace{\lambda^2, \ldots, \lambda^2}^{2n \text{ times}} .$$

Therefore the eigenvalues of $M\mathbf{q}$ are 1, 2-fold λ, $2n$-fold λ^2. Numerical calculation shows that for $n = 5, \ldots, 10$ the largest absolute value of eigenvalues of $M_{\mathbf{d}}$ is less than 0.13621. Since we fix $\lambda := \frac{1}{2}$, we have $0.13621 < 0.25 = \lambda^2$. This implies that QAS^4_+ generates surfaces of bounded curvature.

Denote by χ^{tr} the characteristic map based truncation to 5 digits after the decimal point. χ^{tr} is visually identical to χ in Section 3 and the numerically checked $\partial_u\chi^{tr} \times \partial_v\chi^{tr} > 0$ confirms injectivity of χ^{tr}. Increasing the calculation accuracy in the refinement derivation of Appendix D, and subsequent limit analysis without truncating yields a sequence of maps converging to χ.

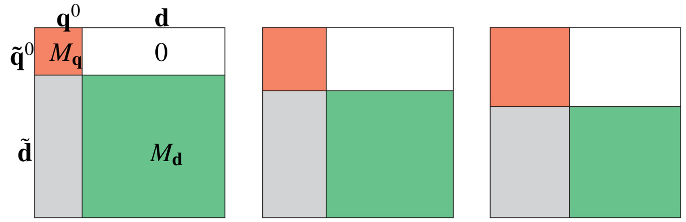

(a) C^2 $\mathbf{q}$ (b) C^1 $\mathbf{q}$ (c) C^1-C^0 $\mathbf{q}$

Figure 12: Matrix M. In all three cases the submatrix $M_{\mathbf{d}}$ is of size $12n \times 12n$. The submatrix $M_{\mathbf{q}}$ is of size: (a) 6×6, (b) $(3+n)\times(3+n)$, (c) $(3+2n)\times(3+2n)$.

6. QAS^3_+: degree bi-3 improved Quadratic-Attraction Subdivision

Fig. 13 shows that the control net refinement of QAS^3 has the same structure as QAS^4, Fig. 9. That is, the $6n$ • in Fig. 13b stem from new refinement rules, and, including those defined by regular, uniform bi-3 C^2 spline refinement rules, one refinement step produces $30n$ new control nodes. For the degree bi-3 there are now 16 4×4 sub-arrangements of the 45 refined nodes to be considered (displayed in Fig. 14a: one of these is surrounded by a red loop, the remaining 15 are obtained by the shifts in one or another direction.) Applying B-to-BB conversion to each of these 16 sub-arrangements yields three 2×2 bi-3 macro-patches, forming one sector of the new ring, see Fig. 14b.

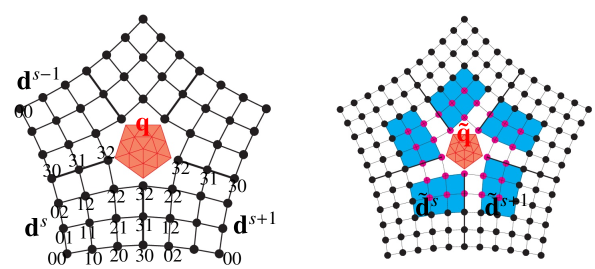

(a) QAS^3: $\mathbf{d}$-net + $\mathbf{q}$ (b) QAS^3 refinement

Figure 13: QAS^3_+: (the only difference to Fig. 9 is the lack of distinction between the control nodes). (a) Labeling of the bi-3 $\mathbf{d}$-net. (b) The nodes marked as • stem from the $\mathbf{d}$-net by regular refinement; new refinement rules define the 6 • nodes per sector. The cyan-underlaid $12n$ nodes $\tilde{\mathbf{d}}^s$, $s = 0, \ldots, n-1$, represent the refined $\mathbf{d}$-net for the next refinement step.

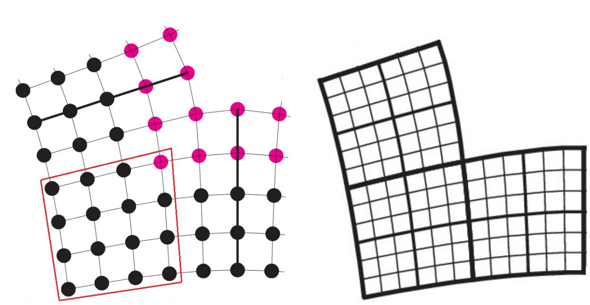

(a) ring1 (b) ring2

Figure 14: QAS^3_+: (a) An arrangement of 45 refined nodes whose B-to-BB conversion yields (b) three 2×2 bi-3 macro-patches of one sector.

We can now summarize the QAS^3_+ algorithm. The $\mathbf{d}$-net is either directly created by the designer or derived from a

Catmull-Clark net according to [5, Fig. 3]. With **p** either given or set by [25, Eq. 2], the central **q** can be directly designed or obtained by applying $(T_3^4)^{-1}$ of Fig. 5 to [5, Sect 4.2].

QAS$^3_+$ Iteration Step. Refine the **d**-net, see Fig. 13, the center quadratic and generate one surface ring.

1. Compute $24n$ nodes marked • by uniform by uniform bi-3 C^2 (B-)spline knot insertion.
2. To compute $6n$ nodes •,
   (a) transform the bi-3 **d**-net to the bi-4 net $\bar{\mathbf{d}}$ with $(T_3^4)^{-1}$;
   (b) apply formulas (6) and (7) of Appendix C to $\bar{\mathbf{d}}$. This yields $\tilde{\bar{\mathbf{d}}}$
   (c) transform bi-4 net $\tilde{\bar{\mathbf{d}}}$ to the bi-3 $\tilde{\mathbf{d}}$ by T_3^4.
3. B-to-BB convert the $30n$ refined nodes to $12n$ bi-3 pieces forming a new surface ring of 2×2 macro-patches as in Fig. 1b.
4. Define $\tilde{\mathbf{q}}$ from **q** by formula (8) of Appendix D.
5. Update $\tilde{\mathbf{q}} \to \mathbf{q}$ and $\tilde{\mathbf{d}} \to \mathbf{d}$.

Subdivision Analysis. Since the subdivision matrix M has the same structure as QAS$^4_+$, the analysis is analogous to Section 5. Numerical calculation for $n = 5, \ldots, 10$ shows the largest absolute eigenvalue of $M_{\mathbf{d}}$ to be less than 0.13626. Therefore QAS$^3_+$ is curvature bounded. For the characteristic map χ^3 of QAS$^3_+$, numerical computation confirms positivity of $\partial_u\chi^3 \times \partial_v\chi^3$, i.e. an injectivity. We also note that each 2×2 bi-3 macro-patch of χ^3 is very similar but not equal to the 2×2 bi-3 macro-patch obtained from one bi-4 patch of χ (Section 3) split into 2×2 sub-patches, extracting the 3×3 jets at the four patch corners in bi-3 form, and completing the bi-3 macro-patch by C^1 averaging. The so-derived bi-3 ring is C^2.

7. Acceleration of QAS$^4_+$ and QAS$^3_+$ to $\lambda < \frac{1}{2}$

QAS^4 inherits the subdominant eigenvalue $\lambda = \frac{1}{2}$ from the refinement of **q** in (8), and the same holds for QAS$^3_+$. If the contraction is accelerated to $\lambda < \frac{1}{2}$, so that $0.13626 < \lambda^2$, the subdivision surface remains curvature bounded and, e.g. for $\lambda := 0.4$, the characteristic map remains injective. However, with decreasing λ, the highlight line distribution becomes less uniform although still better than [20] for $\lambda = 0.4$: Fig. 15 compares the characteristic maps of the $\lambda = 0.4$-accelerated QAS$^3_{0.4}$ (black) to [20] (red) for $n = 5, \ldots, 10$. Visually both BB-nets look acceptable, but the subdivision surfaces reveal stark differences that increase with valence n. That is, good planar shape is necessary but not sufficient for high surface quality.

In subdivision, the first few rings can be treated as determining macroscopic shape. Since already $\lambda = 0.4$ impairs the surface quality, we change λ gradually, for always two steps, from $\lambda = 0.5$ to $\lambda = 0.475$ to $\lambda = 0.45$ before settling for $\lambda = 0.4$ in subsequent steps. The resulting QAS$^4_{0.5..0.4}$ and QAS$^3_{0.5..0.4}$ have only subtly worse shape than QAS$^4_+$ and QAS$^3_+$.

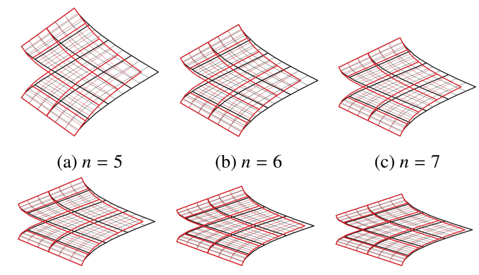

(a) $n = 5$ (b) $n = 6$ (c) $n = 7$
(d) $n = 8$ (e) $n = 9$ (f) $n = 10$

Figure 15: The characteristic maps: black of QAS$^3_{0.4}$ red of [20].

8. Comparisons and Discussion

Subdivision 'tuning', i.e. the adjustment of refinement rules to set eigenvalues, typically neglects the (visually dominant) global surface shape in order to improve limit behavior at the extraordinary point. By contrast, guided surfacing prioritises global shape and obtains good limit properties as a by-product. In the following examples an extended **c**-net, displayed in Fig. 2a, forms the input. Fig. 16 shows a gallery of challenge nets and the outcome, the surrounding bi-3 ring plus the subdivision surface of 10 contracting rings. Note that (colored) shading is not a good surface analysis tool since it does not reliably reveal shape artifacts. Since [22] and [20] are bicubic, we compare to QAS$^3_+$ that has the same layout and bi-degree. QAS$^4_+$ generates still slightly better highlight line distributions.

Highlight lines, [30], are a common tool to asses surface quality. The more uniform, apart from explicit design features, the better. Fig. 18 through Fig. 24 show the highlight line distribution of the surfaces in Fig. 16. A second row zooms in on rings 7–10, unless the quality comparison is obvious already in the large. Since curvature distribution is typically less informative than highlight line distribution, we mostly omit a third row that visualizes curvature (Gauss curvature in Fig. 18 and mean curvature in Fig. 22) but in some cases provide the range to indicate fluctuation bounds.

Fig. 18 through Fig. 24 support the *quality ranking from best to worst* as: QAS$^3_+$,QAS$^3_{0.5..0.4}$, [22], with QAS$^3_{0.4}$ and [20] often equally poor. An exception are 5-valent configurations, such as Fig. 16a: Fig. 17 shows [22] perform on par with QAS$^3_+$. Fig. 18 reveals perfectly uniform highlight lines, even in zoom, for QAS$^3_+$, while [20] and QAS$^3_{0.4}$ have pinching highlight lines near the extraordinary point. Zooming in towards the extraordinary point reveals slight, undesirable highlight line oscillations also for [22]. These observations are reinforced by the shape interrogation in Fig. 19 and Fig. 20 and are so evident in Fig. 21 that a comparison the last four rings can be omitted. Fig. 22 shows QAS$^3_{0.4}$ performing slightly better than [20] and this impression is confirmed by higher valences in Fig. 23 and Fig. 24.

8.1. Discussion

Empirically, QAS$^4_+$ and QAS$^3_+$ have uniform highlight line distributions often in the large and typically in the limit, yet slightly worse than QAS [5]. Here we investigate, whether and how this is an unavoidable price to pay for accelerating convergence. Analogous to the reduction of λ below 0.5, we can

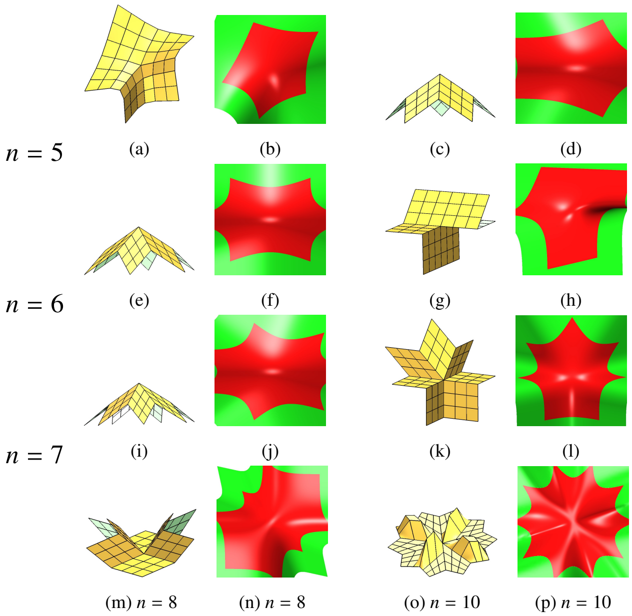

Figure 16: A gallery of extended **c**-nets and the corresponding surface layout. Colored-shading is not a reliable to reveal shape blemishes.

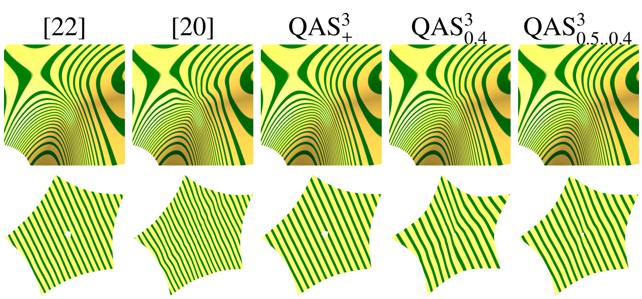

Figure 17: Input net: Fig. 16(a), asymmetric two-beam corner. Row 1: highlight line distribution of the view of Fig. 16(b) Row 2: zoom to inner rings 7–10.

gradually transition from λ_{CC} to $\lambda = \frac{1}{2}$, i.e.

$$\lambda_s := (1 - \frac{s}{K+1})\lambda_{CC} + \frac{s}{K+1}\frac{1}{2} \text{ for } s = 1, \ldots, K \qquad (4)$$

and $\lambda_s := \frac{1}{2}$ for $s > K$. The refinement rules $\mathbb{r}_s$ at step s are an average of $\mathbb{r}_C$ of Appendix C ((6) and (7)) and the rule $\mathbb{r}_Q$ of [5]:

$$\mathbb{r}_s := \omega_s \mathbb{r}_C + (1 - \omega_s)\mathbb{r}_Q, \quad \omega_s := \frac{\lambda_{CC} - \lambda_s}{\lambda_{CC} - \frac{1}{2}}. \qquad (5)$$

The convex parabolic net Fig. 25a with planar sectors brings out the subtle improvement: Fig. 26a,b display a top view of surface Fig. 25b to show how QAS^3_+ contracts slightly faster than [5]. Focusing on Fig. 26 the highlight line distribution of (d) reveals slight oscillations already in the first ring, whereas those of (c), according to [5], are perfect. The average rule (g) with $K = 6$ steps improves on (d), but not on (c) [5]. That is, the higher speed still exerts a cost, although much diminished. The middle row of Fig. 26 demonstrates the importance of averaging the rules: the surfaces are the result of gradual change of λ_s according to (4) and setting, for $s > K$, $\mathbb{r}_s := \mathbb{r}_C$. but with

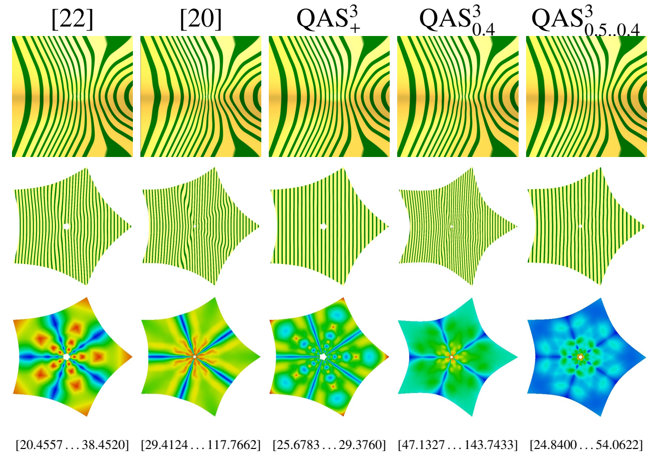

Figure 18: Input net: Fig. 16(c) Row 1: highlight line distribution of the view of Fig. 16(d) Row 2: zoom to inner rings 7–10. Row 3: Gauss curvature with range below.

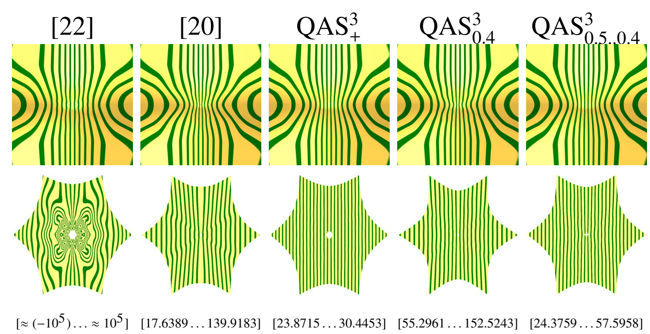

Figure 19: Input net: Fig. 16(e) Row 1: highlight line distribution of the view of Fig. 16(f) Row 2: zoom to inner rings 7–10, rotated by $\frac{\pi}{2}$. Row 3: Gaussian curvature ranges (no figures).

different settings of $\mathbb{r}$ for $s \leq K$ as follows: (e) uses fixed $\mathbb{r}_Q$, (f) uses fixed $\mathbb{r}_C$, (g) uses rules $\mathbb{r}_s$ averaged according to Eq. (5). (g) has clearly the best highlight line distribution. The bottom row shows the poorer quality of the alternative approaches.

The subtle price paid by accelerating contraction is also the topic of Fig. 27, for surfaces obtained from Fig. 25c. The highlight lines of QAS^3 in Fig. 27b are perfect but those of QAS^3_+ oscillate near the extraordinary point. Averaging with $K = 3$ improves the quality. The number K of modified rings depends on application. Empirically, $K = 6$ is sufficient even for extreme configurations. Throughout, the Algorithm is unchanged except for substituting λ_s and $\mathbb{r}_s$. The bi-4 surfaces QAS^4_+ can be improved analogously.

9. Conclusion

A subdominant eigenvalue of $\lambda > 0.5$ is observed both for $n > 4$ and classic generalized subdivision, as well as high-quality modern subdivision. Compared to uniform tensor-product spline refinement, where $\lambda = 0.5$, the larger λ reduces convergence and creates a mismatch between binary refinement and contraction of the surface rings. Direct tuning of the subdominant eigenvalue λ as contraction speed results in poorer

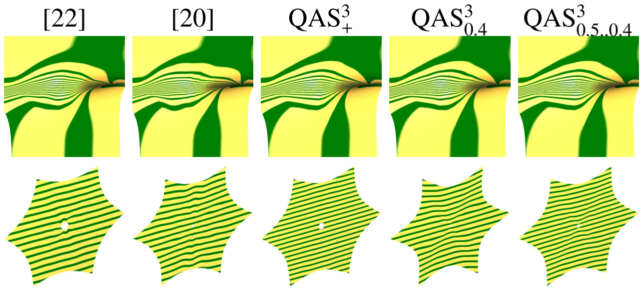

Figure 20: Input net: Fig. 16(g). Row 1: highlight line distribution of the view of Fig. 16(h) Row 2: zoom to inner rings 7–10.

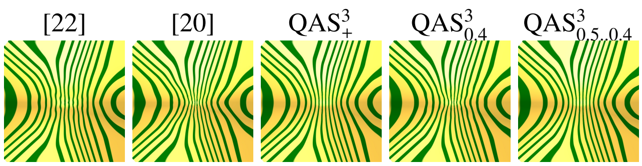

Figure 21: Input net: Fig. 16(i). highlight line distribution.

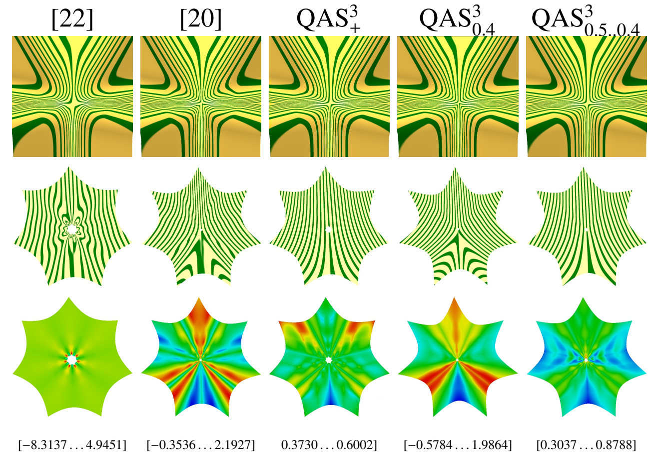

Figure 22: Input net: Fig. 16(k). highlight line distribution, zoom to rings 7–10, mean curvature and curvature range.

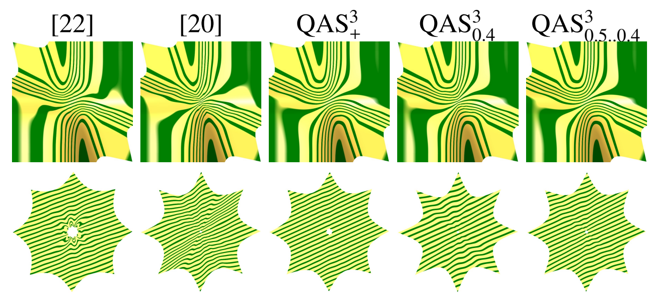

Figure 23: Input net: Fig. 16(m) of valence 8. The highlight lines for column [22], and to a lesser degree in [20] and QAS$^3_{0.4}$, oscillate; for QAS$^3_{0.4}$they are additionally pulled towards the extraordinary point. While highlight lines in QAS$^3_+$ and QAS$^3_{0.5..0.4}$ look alike from afar, their zoom show those of QAS$^3_{0.5..0.4}$ to be less uniform than those of QAS$^3_+$, where oscillations are extremely mild.

surfaces, characterized by an uneven distribution and oscillation of highlight lines. These shortcomings are remedied by the improvement QAS$_+$ of QAS. QAS$_+$ provides good shape with the uniform $\lambda = \frac{1}{2}$ contraction of the tensor-product case. An implementation of QAS$^3_+$ is available at [26] under the branch ‘equi-spaced’.

Acknowledgements Kyle Lo helped with the code distribution.

References

[1] E. Catmull, J. Clark, Recursively generated B-spline surfaces on arbitrary topological meshes, Computer-Aided Design 10 (1978) 350–355.

[2] C. De Boor, K. Höllig, S. Riemenschneider, Box splines, Vol. 98, Springer Science & Business Media, 2013.

[3] H. Prautzsch, A short proof of the oslo algorithm, Computer Aided Geometric Design 1 (1) (1984) 95–96.

[4] U. H. Augsdörfer, N. A. Dodgson, M. A. Sabin, Tuning subdivision by minimising gaussian curvature variation near extraordinary vertices, Computer Graphics Forum 25 (3) (2006) 263–272.

[5] K. Karčiauskas, J. Peters, Quadratic-attraction subdivision, Computer Graphics Forum 42 (5) (2023) e14 900.

[6] G. J. Hettinga, J. Kosinka, A multisided C^2 B-spline patch over extraordinary vertices in quadrilateral meshes, Comput. Aided Des 127 (2020) 102855.

[7] M. Vaitkus, T. Várady, P. Salvi, Á. Sipos, Multi-sided b-spline surfaces over curved, multi-connected domains, Computer Aided Geometric Design 89 (2021) 102019.

[8] X. Gu, Y. He, H. Qin, Manifold splines, in: Proceedings of the 2005 ACM symposium on Solid and physical modeling, 2005, pp. 27–38.

[9] C. T. Loop, S. Schaefer, G^2 tensor product splines over extraordinary vertices, Comput. Graph. Forum 27 (5) (2008) 1373–1382.

[10] G.-P. Bonneau, S. Hahmann, Flexible G^1 interpolation of quad meshes, Graphical Models 76 (6) (2014) 669–681.

[11] M. Kapl, G. Sangalli, T. Takacs, Dimension and basis construction for analysis-suitable g^1 two-patch parameterizations, Computer Aided Geometric Design 52-53 (2017) 75–89.

[12] M. Marsala, A. Mantzaflaris, B. Mourrain, G1-smooth biquintic approximation of Catmull-Clark subdivision surfaces, Computer Aided Geometric Design 99 (2022) 102158.

[13] P. R. Pfluger, M. Neamtu, On degenerate surface patches, Numerical Algorithms 5 (1993) 569–575.

[14] U. Reif, A refineable space of smooth spline surfaces of arbitrary topological genus, Journal of Approximation Theory 90 (2) (1997) 174–199.

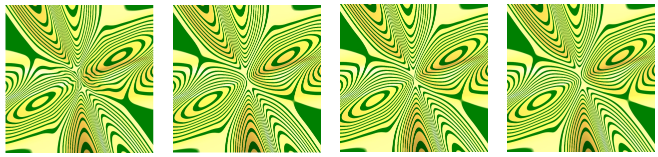

(a) [20] (b) QAS^3_+ (c) $\mathrm{QAS}^3_{0.4}$ (d) $\mathrm{QAS}^3_{0.5..0.4}$

(e) [20] (f) QAS^3_+ (g) $\mathrm{QAS}^3_{0.4}$ (h) $\mathrm{QAS}^3_{0.5..0.4}$

Figure 24: Input net: Fig. 16(m) of valence 10. The highlight lines in (a,e) oscillate whereas (b), (c), (d) look uniform except for (c) pulled towards the extraordinary point. The zoom shows decreasing oscillations in (g), (h) and (f).

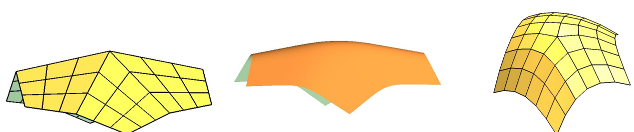

(a) **c**-net, $n = 6$ (b) expected surface shape for (a) (c) **c**-net, $n = 5$

Figure 25: Challenge configurations.

[15] J. A. Gregory, Smooth interpolation without twist constraints, Academic Press, 1974, pp. 71–88.

[16] M. A. Sabin, C. Fellows, J. Kosinka, Cad model details via curved knot lines and truncated powers, Computer-Aided Design 143 (2022) 103137.

[17] J. Peters, Splines for meshes with irregularities, The SMAI journal of computational mathematics S5 (2019) 161–183.

[18] D. Doo, M. Sabin, Behaviour of recursive division surfaces near extraordinary points, Computer-Aided Design 10 (1978) 356–360.

[19] J. Stam, Exact evaluation of catmull-clark subdivision surfaces at arbitrary parameter values, in: Proceedings of the 25th annual conference on Computer graphics and interactive techniques, 1998, pp. 395–404.

[20] X. Wang, W. Ma, An extended tuned subdivision scheme with optimal convergence for isogeometric analysis, Computer-Aided Design 162 (2023) 103544.

[21] Y. Ma, W. Ma, Subdivision schemes with optimal bounded curvature near extraordinary vertices, Computer Graphics Forum 37 (7) (2018) 455–467.

[22] Y. Ma, W. Ma, Subdivision schemes for quadrilateral meshes with the least polar artifact in extraordinary regions, Comput. Graph. Forum 38 (7) (2019) 127–139.

[23] X. Li, X. Wei, Y. J. Zhang, Hybrid non-uniform recursive subdivision with improved convergence rates, Computer Methods in Applied Mechanics and Engineering 352 (2019) 606–624.

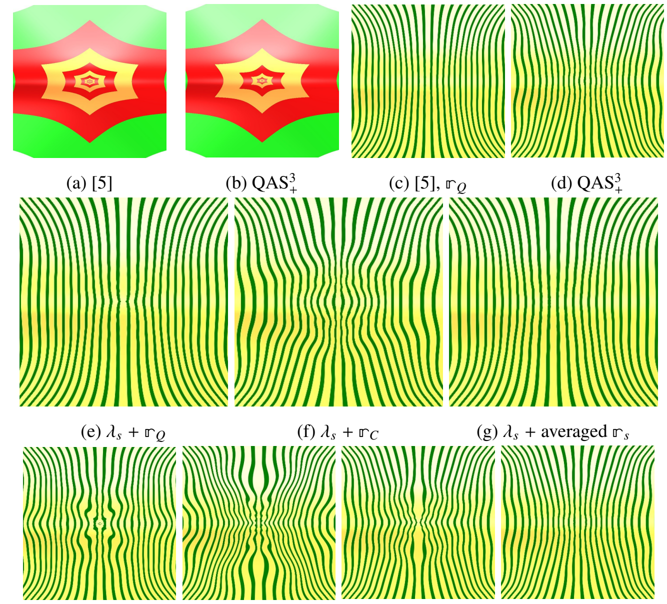

(a) [5] (b) QAS^3_+ (c) [5], $\mathbb{r}_Q$ (d) QAS^3_+

(e) $\lambda_s + \mathbb{r}_Q$ (f) $\lambda_s + \mathbb{r}_C$ (g) λ_s + averaged $\mathbb{r}_s$

(h) [22] (i) [20] (j) $\mathrm{QAS}^3_{0.4}$ (k) $\mathrm{QAS}^3_{0.5..0.4}$

Figure 26: Surfaces from input Fig. 25a, top view. Zoom on rings 7-10.

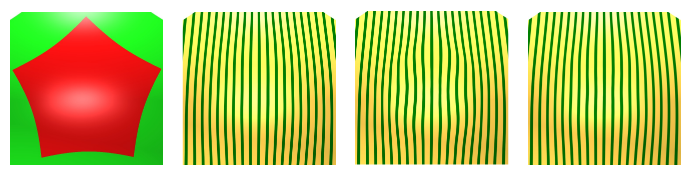

(a) view (b) [5] (c) QAS^3_+ (d) averaged $\mathbb{r}_s$

Figure 27: Surfaces from **c**-net Fig. 25c.

[24] X. Wei, X. Li, Y. J. Zhang, T. J. Hughes, Tuned hybrid nonuniform subdivision surfaces with optimal convergence rates, International Journal for Numerical Methods in Engineering 122 (9) (2021) 2117–2144.

[25] K. Karčiauskas, J. Peters, Point-augmented bi-cubic subdivision surfaces, Computer Graphics Forum 41 (7) (2023) 13–23.

[26] J. Peters, K. Lo, K. Karčiauskas, Quadratic-attraction subdivision, C++ code, `https://bitbucket.org/surflab/quadratic-attraction-subdivision`.

[27] C. de Boor, B-form basics, in: G. Farin (Ed.), Geometric Modeling: Algorithms and New Trends, SIAM, 1987, pp. 131–148.

[28] G. Farin, Curves and Surfaces for Computer Aided Geometric Design: A Practical Guide, Academic Press, 1988.

[29] K. Karčiauskas, J. Peters, Evolving guide subdivision, in: Eurographics 2023, 2023.

[30] K.-P. Beier, Y. Chen, Highlight-line algorithm for realtime surface-quality assessment, Comp-Aid Design 26 (4) (1994) 268–277.

Appendix A: The scalars ν

The Table below lists:
from left to right the coefficients $\nu_2^i, \nu_3^i, \nu_4^i, \nu_6^i, \dot{\nu}^i$;
from top to bottom $i = 5, 7, 8, 9, 10$.

127(1571+1320c)	4(70789+18832c)	−(5977+14260c)	−19824s	2ĉ(24779+1240c)
−2667(793+40c)	3116(793+40c)	7(35871−6548c)	−316848s	4ĉ(18027+586c)
−53340s	62320s	9440s	42(7733+3772c)	−ŝ(15837−1172c)
−2667(1387+132c)	3116(1387+132c)	3(177155−804c)	−501984s	14ĉ(80389−372c)
−88011s	102828s	15576s	21(13199+5976c)	−7ŝ(4613+186c)

Appendix B: The scalars z_3, z_4, z_6

In Table below lists:
from left to right $n = 5, 6, 7, 8, 9, 10$;
from top to bottom z_3, z_4, z_6.

1.0523486064	1.0479628065	1.0453666602	1.0437024506	1.0425713792	1.0417674430
0.6835325141	0.6712282471	0.6639841979	0.6593541908	0.6562128317	0.6539824091
0.1409618117	0.1171902825	0.1002802002	0.0876392989	0.0778325682	0.0700027016

Appendix C: Explicit formulas of the refined net: $\tilde{\mathbf{d}}_{ij}^s$, $i = 1, 2, 3$, $j = 1, 2$ in terms of d, q and p

Note, that the structure of Tables K and T is the same as in [5]. For $s = 0, \ldots, n-1$ and $j = 1, 2$,

$$\begin{aligned}\tilde{\mathbf{d}}_{3j}^s := &\sum_{r=-1}^{2}\sum_{m=0}^{2}\sum_{l=0}^{3}\kappa_{lm}^s \mathbf{d}_{lm}^{s+r} + \frac{1}{2}\sum_{k=2}^{6}\tau_{3j,k}\mathbf{q}_k^s + \frac{1}{2}(\tau_{3j,2}\mathbf{q}_4^{s+1} + \\ &\tau_{3j,3}\mathbf{q}_6^{s+1} + \tau_{3j,4}\mathbf{q}_2^{s+1} + \tau_{3j,5}\mathbf{q}_5^{s+1} + \tau_{3j,6}\mathbf{q}_3^{s+1}) + \\ &(1 - \sum_{r=-1}^{2}\sum_{m=0}^{2}\sum_{l=0}^{3}\kappa_{lm}^s - \sum_{k=2}^{6}\tau_{3j,k})\mathbf{p}\,.\end{aligned} \tag{6}$$

$$\begin{aligned}\tilde{\mathbf{d}}_{ij}^s := &\sum_{r=-1}^{1}\sum_{m=0}^{2}\sum_{l=0}^{3}\kappa_{lm}^s \mathbf{d}_{lm}^{s+r} + \sum_{k=2}^{6}\tau_{ij,k}\mathbf{q}_k^s + \\ &(1 - \sum_{r=-1}^{1}\sum_{m=0}^{2}\sum_{l=0}^{3}\kappa_{lm}^s - \sum_{k=2}^{6}\tau_{ij,k})\mathbf{p}, \quad i = 1, 2.\end{aligned} \tag{7}$$

Here the index r enumerates the sectors with respect to the current sector s, namely s for $r = 0$ and the previous one for $r = -1$. Since only information from *some* of the neighboring sectors is needed, r remains in $\{-1, 0, 1, 2\}$. The tables T_n

$$T_n := 10^5 \begin{pmatrix} \tau_{11,2} & \tau_{11,3} & \tau_{11,4} & \tau_{11,5} & \tau_{11,6} \\ \tau_{22,2} & \tau_{22,3} & \tau_{22,4} & \tau_{22,5} & \tau_{22,6} \\ \tau_{21,2} & \tau_{21,3} & \tau_{21,4} & \tau_{21,5} & \tau_{21,6} \\ \tau_{12,2} & \tau_{12,3} & \tau_{12,4} & \tau_{12,5} & \tau_{12,6} \\ \tau_{31,2} & \tau_{31,3} & \tau_{31,4} & \tau_{31,5} & \tau_{31,6} \\ \tau_{32,2} & \tau_{32,3} & \tau_{32,4} & \tau_{32,5} & \tau_{32,6} \end{pmatrix}.$$

encode the stencil weights $\tau_{ij,k}$, where $_{ij}$ indicates a location of refined node $\tilde{\mathbf{d}}_{ij}^s$ in sector s and $_k$ labels the weights of the quadratic expansion coefficient $\mathbf{q}_k^s$.

For the tables K see Fig. 28. Fig. 28a displays K consisting of the four groups κ_{ij}^r, $r = -1, 0, 1, 2$ in formulas (7) and (6) arranged around a filler $\mathbf{0}$ in the center. Since even in this compact grouping many weights κ_{ij}^r (scaled by 10^5) are 0, we focus on pieces of K. For $l = 1, 2$, Fig. 28b displays the only nonzero 5×5 matrices K_{lm}^n, where lm, $m = 1, 2$ is the index of the refined node $\tilde{\mathbf{d}}_{lm}^s$. For $l = 3$, Fig. 28c shows the only nonzero entries dark and light underlaid. The weights are symmetric across the center line so that only the left (darker underlaid) 5×4 matrices K_{3m}^n, $m = 1, 2$, are given.

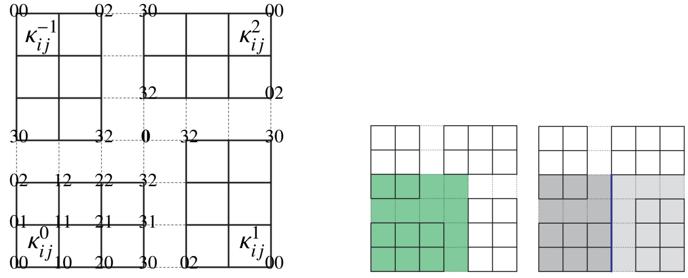

(a) labels of coefficients κ_{ij}^k (b) 5×5 K (c) 5×4 K

Figure 28: Structure of matrices K^n, $n > 4$. (a) Labels of all coefficients κ_{ij}^k, $i = 0, \ldots, 3$, $j = 0, 1, 2$, $k = -1, 0, 1, 2$. (b) K_{11}^n, K_{21}^n, K_{12}^n, K_{22}^n. (c) left darker: K_{31}^n, K_{32}^n.

$$T_5 := \begin{pmatrix} -3715 & 9388 & -3715 & 6533 & 9388 \\ 10340 & 17595 & 10340 & 30888 & 17595 \\ -134 & 3365 & -5290 & 17973 & 28682 \\ -5290 & 28682 & -134 & 17973 & 3365 \\ 4650 & -3365 & 10871 & 2079 & 48454 \\ 24316 & -17595 & 38634 & 10874 & 42415 \end{pmatrix}$$

$$K_{11}^5 := \begin{pmatrix} -18 & -183 & -1601 & 0 & 0 \\ 92 & 2414 & 5374 & 0 & 0 \\ 47 & 8756 & 50302 & 5374 & -1601 \\ 10 & 1690 & 8756 & 2414 & -183 \\ 10 & 10 & 47 & 92 & -18 \end{pmatrix}, \; K_{22}^5 := \begin{pmatrix} 1 & 135 & -1383 & 0 & 0 \\ 2 & 245 & 1635 & 0 & 0 \\ -5 & 81 & 11827 & 1635 & -1383 \\ 0 & 35 & 81 & 245 & 135 \\ 1 & 0 & -5 & 2 & 1 \end{pmatrix}$$

$$K_{21}^5 := \begin{pmatrix} -2 & -61 & -886 & 0 & 0 \\ 0 & 398 & 1106 & 0 & 0 \\ -12 & 606 & 30422 & 13539 & -523 \\ -4 & 113 & 6524 & 4546 & 1073 \\ 2 & 14 & -31 & 12 & 17 \end{pmatrix}, \; K_{12}^5 := \begin{pmatrix} 17 & 1073 & -523 & 0 & 0 \\ 12 & 4546 & 13539 & 0 & 0 \\ -31 & 6524 & 30422 & 1106 & -886 \\ 14 & 113 & 606 & 398 & -61 \\ 2 & -4 & -12 & 0 & -2 \end{pmatrix}$$

$$K_{31}^5 := \begin{pmatrix} 1 & 30 & 443 & 0 \\ 0 & -199 & -553 & 0 \\ 6 & -303 & 3800 & 23960 \\ 2 & -56 & 2450 & 7953 \\ -1 & -7 & 6 & -12 \end{pmatrix}, \; K_{32} := \begin{pmatrix} 0 & -67 & 691 & 0 \\ -1 & -122 & -817 & 0 \\ 2 & -40 & -3659 & 1489 \\ 0 & -17 & -108 & -245 \\ 0 & 0 & 2 & -2 \end{pmatrix}$$

$$T_6 := \begin{pmatrix} -3323 & 9745 & -3323 & 6690 & 9745 \\ 13325 & 14205 & 13325 & 30135 & 14205 \\ 957 & 2442 & -3220 & 18647 & 27112 \\ -3220 & 27112 & 957 & 18647 & 2442 \\ 2442 & -2442 & 11808 & 2442 & 45676 \\ 14205 & -14205 & 39279 & 14205 & 36540 \end{pmatrix}$$

$$K_{11}^6 := \begin{pmatrix} -15 & -239 & -1766 & 0 & 0 \\ 138 & 2858 & 5297 & 0 & 0 \\ 64 & 8487 & 48965 & 5297 & -1766 \\ 13 & 1753 & 8487 & 2858 & -239 \\ 15 & 13 & 64 & 138 & -15 \end{pmatrix}, \; K_{22}^6 := \begin{pmatrix} 1 & 179 & -986 & 0 & 0 \\ 2 & 311 & 1558 & 0 & 0 \\ -8 & 98 & 10646 & 1558 & -986 \\ 0 & 52 & 98 & 311 & 179 \\ 1 & 0 & -8 & 2 & 1 \end{pmatrix}$$

$$K_{21}^6 := \begin{pmatrix} 0 & -98 & -891 & 0 & 0 \\ 3 & 557 & 1027 & 0 & 0 \\ -14 & 871 & 29275 & 13151 & -403 \\ -6 & 166 & 6276 & 4465 & 1212 \\ 3 & 21 & -46 & 9 & 22 \end{pmatrix}, \; K_{12}^6 := \begin{pmatrix} 22 & 1212 & -403 & 0 & 0 \\ 9 & 4465 & 13151 & 0 & 0 \\ -46 & 6276 & 29275 & 1027 & -891 \\ 21 & 166 & 871 & 557 & -98 \\ 3 & -6 & -14 & 3 & 0 \end{pmatrix}$$

$$K_{31}^6 := \begin{pmatrix} 0 & 49 & 445 & 0 \\ -1 & -278 & -513 & 0 \\ 7 & -435 & 4313 & 24348 \\ 3 & -83 & 2505 & 8034 \\ -1 & -10 & 11 & -9 \end{pmatrix}, \; K_{32}^6 := \begin{pmatrix} 0 & -89 & 493 & 0 \\ -1 & -155 & -779 & 0 \\ 4 & -49 & -3267 & 1566 \\ 0 & -26 & -138 & -311 \\ 0 & 0 & 3 & -2 \end{pmatrix}$$

$$T_7 := \begin{pmatrix} -3144 & 10071 & -3144 & 6885 & 10071 \\ 14803 & 12463 & 14803 & 29570 & 12463 \\ 1416 & 2179 & -1760 & 18891 & 25990 \\ -1760 & 25990 & 1416 & 18891 & 2179 \\ 1641 & -2179 & 12550 & 2718 & 43869 \\ 9385 & -12463 & 41671 & 15542 & 32325 \end{pmatrix}$$

$$K_{11}^7 := \begin{pmatrix} -10 & -263 & -1877 & 0 & 0 \\ 163 & 3113 & 5196 & 0 & 0 \\ 72 & 8339 & 48055 & 5196 & -1877 \\ 13 & 1789 & 8339 & 3113 & -263 \\ 19 & 13 & 72 & 163 & -10 \end{pmatrix}, \; K_{22}^7 := \begin{pmatrix} 2 & 198 & -778 & 0 & 0 \\ 1 & 334 & 1488 & 0 & 0 \\ -9 & 100 & 9952 & 1488 & -778 \\ 0 & 62 & 100 & 334 & 198 \\ 2 & 0 & -9 & 1 & 2 \end{pmatrix}$$

$$K_{21}^7 := \begin{pmatrix} 1 & -122 & -922 & 0 & 0 \\ 8 & 638 & 944 & 0 & 0 \\ -13 & 1015 & 28614 & 12936 & -315 \\ -7 & 196 & 6134 & 4411 & 1289 \\ 3 & 25 & -54 & 4 & 23 \end{pmatrix}, \; K_{12}^7 := \begin{pmatrix} 23 & 1289 & -315 & 0 & 0 \\ 4 & 4411 & 12936 & 0 & 0 \\ -54 & 6134 & 28614 & 944 & -922 \\ 25 & 196 & 1015 & 638 & -122 \\ 3 & -7 & -13 & 8 & 1 \end{pmatrix}$$

$$K_{31}^7 := \begin{pmatrix} 0 & 61 & 461 & 0 \\ -4 & -319 & -472 & 0 \\ 6 & -507 & 4600 & 24563 \\ 3 & -98 & 2538 & 8088 \\ -1 & -12 & 15 & -4 \end{pmatrix}, \; K_{32}^7 := \begin{pmatrix} -1 & -99 & 389 & 0 \\ 0 & -167 & -744 & 0 \\ 4 & -50 & -3024 & 1636 \\ 0 & -31 & -149 & -334 \\ -1 & 0 & 3 & -1 \end{pmatrix}$$

$$T_8 := \begin{pmatrix} -3049 & 10311 & -3049 & 7030 & 10311 \\ 15648 & 11438 & 15648 & 29171 & 11438 \\ 1649 & 2105 & -748 & 18994 & 25206 \\ -748 & 25206 & 1649 & 18994 & 2105 \\ 1233 & -2105 & 13108 & 2977 & 42590 \\ 6700 & -11438 & 43807 & 16176 & 29412 \end{pmatrix}$$

$$K_{11}^8 := \begin{pmatrix} -6 & -274 & -1951 & 0 & 0 \\ 179 & 3271 & 5120 & 0 & 0 \\ 77 & 8249 & 47436 & 5120 & -1951 \\ 13 & 1811 & 8249 & 3271 & -274 \\ 21 & 13 & 77 & 179 & -6 \end{pmatrix}, \; K_{22}^8 := \begin{pmatrix} 2 & 208 & -653 & 0 & 0 \\ 1 & 343 & 1435 & 0 & 0 \\ -10 & 99 & 9510 & 1435 & -653 \\ -1 & 69 & 99 & 343 & 208 \\ 2 & -1 & -10 & 1 & 2 \end{pmatrix}$$

$$K_{21}^8 := \begin{pmatrix} 2 & -137 & -952 & 0 & 0 \\ 11 & 686 & 880 & 0 & 0 \\ -13 & 1102 & 28198 & 12803 & -252 \\ -8 & 214 & 6044 & 4375 & 1335 \\ 4 & 27 & -59 & 0 & 23 \end{pmatrix}, \; K_{12}^8 := \begin{pmatrix} 23 & 1335 & -252 & 0 & 0 \\ 0 & 4375 & 12803 & 0 & 0 \\ -59 & 6044 & 28198 & 880 & -952 \\ 27 & 214 & 1102 & 686 & -137 \\ 4 & -8 & -13 & 11 & 2 \end{pmatrix}$$

$$K_{31}^8 := \begin{pmatrix} -1 & 68 & 476 & 0 \\ -5 & -343 & -440 & 0 \\ 6 & -551 & 4776 & 24696 \\ 4 & -107 & 2559 & 8124 \\ -2 & -13 & 17 & 0 \end{pmatrix}, \; K_{32}^8 := \begin{pmatrix} -1 & -104 & 326 & 0 \\ 0 & -171 & -717 & 0 \\ 5 & -49 & -2866 & 1689 \\ 0 & -34 & -153 & -343 \\ -1 & 0 & 4 & -1 \end{pmatrix}$$

$$T_9 := \begin{pmatrix} -2991 & 10484 & -2991 & 7133 & 10484 \\ 16180 & 10778 & 16180 & 28886 & 10778 \\ 1782 & 2092 & -31 & 19042 & 24647 \\ -31 & 24647 & 1782 & 19042 & 2092 \\ 979 & -2092 & 13544 & 3205 & 41642 \\ 5043 & -10778 & 45481 & 16513 & 27359 \end{pmatrix}$$

$$K_{11}^9 := \begin{pmatrix} -2 & -281 & -2001 & 0 & 0 \\ 190 & 3377 & 5066 & 0 & 0 \\ 81 & 8189 & 47001 & 5066 & -2001 \\ 13 & 1826 & 8189 & 3377 & -281 \\ 22 & 13 & 81 & 190 & -2 \end{pmatrix}, \; K_{22}^9 := \begin{pmatrix} 2 & 213 & -571 & 0 & 0 \\ 1 & 347 & 1395 & 0 & 0 \\ -10 & 98 & 9210 & 1395 & -571 \\ -1 & 73 & 98 & 347 & 213 \\ 2 & -1 & -10 & 1 & 2 \end{pmatrix}$$

$$K_{21}^9 := \begin{pmatrix} 3 & -147 & -976 & 0 & 0 \\ 13 & 718 & 833 & 0 & 0 \\ -12 & 1160 & 27919 & 12714 & -207 \\ -8 & 227 & 5983 & 4349 & 1366 \\ 4 & 28 & -62 & -2 & 23 \end{pmatrix}, \; K_{12}^9 := \begin{pmatrix} 23 & 1366 & -207 & 0 & 0 \\ -2 & 4349 & 12714 & 0 & 0 \\ -62 & 5983 & 27919 & 833 & -976 \\ 28 & 227 & 1160 & 718 & -147 \\ 4 & -8 & -12 & 13 & 3 \end{pmatrix}$$

$$K_{31}^9 := \begin{pmatrix} -1 & 73 & 488 & 0 \\ -6 & -359 & -416 & 0 \\ 6 & -580 & 4894 & 24785 \\ 4 & -113 & 2574 & 8150 \\ -2 & -14 & 19 & 2 \end{pmatrix}, \; K_{32}^9 := \begin{pmatrix} -1 & -106 & 285 & 0 \\ 0 & -173 & -697 & 0 \\ 5 & -49 & -2756 & 1729 \\ 0 & -36 & -155 & -347 \\ -1 & 0 & 4 & -1 \end{pmatrix}$$

$$T_{10} := \begin{pmatrix} -2954 & 10611 & -2954 & 7208 & 10611 \\ 16538 & 10327 & 16538 & 28676 & 10327 \\ 1865 & 2100 & 490 & 19066 & 24237 \\ 490 & 24237 & 1865 & 19066 & 2100 \\ 802 & -2100 & 13893 & 3399 & 40920 \\ 3944 & -10327 & 46764 & 16710 & 25870 \end{pmatrix}$$

$$K_{11}^{10} := \begin{pmatrix} 0 & -285 & -2037 & 0 & 0 \\ 197 & 3451 & 5026 & 0 & 0 \\ 83 & 8147 & 46686 & 5026 & -2037 \\ 12 & 1836 & 8147 & 3451 & -285 \\ 23 & 12 & 83 & 197 & 0 \end{pmatrix}, \; K_{22}^{10} := \begin{pmatrix} 2 & 217 & -515 & 0 & 0 \\ 0 & 348 & 1365 & 0 & 0 \\ -11 & 96 & 8997 & 1365 & -515 \\ -1 & 76 & 96 & 348 & 217 \\ 2 & -1 & -11 & 0 & 2 \end{pmatrix}$$

$$K_{21}^{10} := \begin{pmatrix} 4 & -154 & -995 & 0 & 0 \\ 15 & 739 & 798 & 0 & 0 \\ -12 & 1200 & 27722 & 12651 & -174 \\ -9 & 236 & 5940 & 4330 & 1387 \\ 4 & 29 & -64 & -5 & 23 \end{pmatrix}, \; K_{12}^{10} := \begin{pmatrix} 23 & 1387 & -174 & 0 & 0 \\ -5 & 4330 & 12651 & 0 & 0 \\ -64 & 5940 & 27722 & 798 & -995 \\ 29 & 236 & 1200 & 739 & -154 \\ 4 & -9 & -12 & 15 & 4 \end{pmatrix}$$

$$K_{31}^{10} := \begin{pmatrix} -2 & 77 & 497 & 0 \\ -7 & -369 & -399 & 0 \\ 6 & -600 & 4975 & 24848 \\ 4 & -118 & 2585 & 8169 \\ -2 & -14 & 20 & 5 \end{pmatrix}, \; K_{32}^{10} := \begin{pmatrix} -1 & -108 & 257 & 0 \\ 0 & -174 & -682 & 0 \\ 5 & -48 & -2678 & 1759 \\ 0 & -38 & -156 & -348 \\ -1 & 0 & 4 & 0 \end{pmatrix}$$

Appendix D: QAS derivation

For completeness,and to motivate the formulas of the refined **d**-net, we summarize the derivation of QAS in [5], using, as much as possible, the same notation to indicate that this part of the QAS$_+$ derivation does not differ from QAS, except for the replacement of χ_{CC} by χ. All calculations of the derivation were performed in symbolic form, since we aim to derive *formulas* for arbitrary input **d**-nets, not numbers for specific input. Fig. 29 outlines the derivation steps.

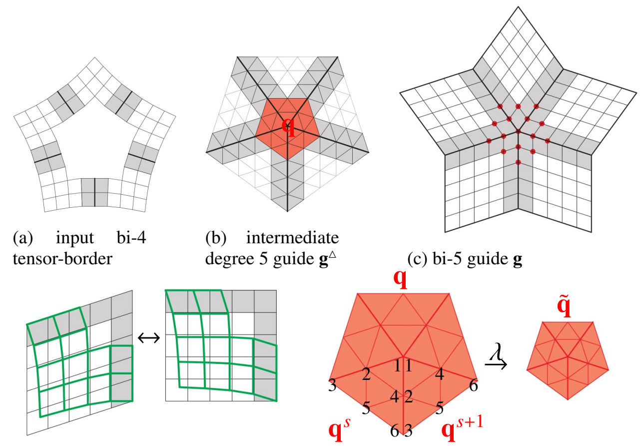

(a) input bi-4 tensor-border (b) intermediate degree 5 guide $\mathbf{g}^\triangle$ (c) bi-5 guide **g** (d) linear transformation L (e) $\tilde{\mathbf{q}} := \lambda\mathbf{q}$

Figure 29: Sketch of derivation.

1. An intermediate guide $\mathbf{g}^\triangle$ of total degree 5 is constructed, see Fig. 29b: the red-underlaid BB-net corresponds to the C^2 quadratic expansion in degree-raised to 5 form; the gray-underlaid BB-coefficients insure C^1 join of adjacent sectors. The $6n$ linearly independent BB-coefficients in the gray part are fixed to match $6n$ linearly independent BB-coefficients of the input bi-4 tensor-border, gray-underlaid inFig. 29a, defined by the **d**-net. (By 'matching', we mean a comparison of the input bi-4 data to the tensor-border obtained via sampling a guide with characteristic tensor-border [5, Sect 3].)

2. The guide $\mathbf{g}^\triangle$ is too rigid to properly join the input bi-4 tensor-border and the resulting subdivision surfaces have poor highlight lines. Therefore $\mathbf{g}^\triangle$ is reparameterized as a bi-5 guide **g** over a larger domain formed by sector parallelograms (see Fig. 29c). Since this tensor-product map is defined on the unit square, this is technically achieved by applying a linear transformation L to the map and the tensor-border $\bar{\chi}$ of the characteristic ring, see Fig. 29d. The gray-underlaid BB-coefficients in Fig. 29c ensure G^1-continuity between sectors.

3. The new layout and the increased number of unconstrained (unmarked) BB-coefficients compared to $\mathbf{g}^\triangle$ allows matching the unmarked BB-coefficients in Fig. 29a: the BB-coefficients • of **g** in Fig. 29c are affine combinations of BB-coefficients of **q** in Fig. 29e. Sampling the composition of the guide **g** yields the tensor-border of the characteristic ring ($\bar{\chi}_{CC}$ in [5], see Fig. 8a, but here $\bar{\chi}$ see Fig. 8c). This allows expressing the remaining BB-coefficients of **g** as affine combinations of BB-coefficients of the quadratic expansion **q** and the nodes of **d**-net.

4. Scaling $\bar{\chi}$ by the subdominant eigenvalue (see Fig. 8b,d) yields the tensor-borders. Sampling and converting them to B-spline form yields $6n$ new nodes in Fig. 9b; the remaining $6n$ sampled nodes are replaced by those obtained from regular refinement (uniform knot insertion).

5. Sampling the guide **g** with $\lambda\bar{\chi}$ is the same as restricting

the $\mathbf{g}$ to to its domain scaled (towards origin) by λ, recalculating the BB-coefficients of the restriction, and then sampling so-'scaled' guide using $\bar{\chi}$. Therefore the new quadratic expansion $\tilde{\mathbf{q}}$ is defined as follows, see Fig. 29e. The $\mathbf{q}$ is restricted to the initial domain scaled by λ. Recalculating BB-coefficients of restriction we get new quadratic expansion $\tilde{\mathbf{q}}$ of (8):

$$\begin{pmatrix} \tilde{\mathbf{q}}_1^s \\ \tilde{\mathbf{q}}_2^s \\ \tilde{\mathbf{q}}_3^s \\ \tilde{\mathbf{q}}_4^s \\ \tilde{\mathbf{q}}_5^s \\ \tilde{\mathbf{q}}_6^s \end{pmatrix} := S \begin{pmatrix} \mathbf{q}_1^s \\ \mathbf{q}_2^s \\ \mathbf{q}_3^s \\ \mathbf{q}_4^s \\ \mathbf{q}_5^s \\ \mathbf{q}_6^s \end{pmatrix}, \ S := \begin{pmatrix} 1 & 0 & 0 & 0 & 0 & 0 \\ 1-\lambda & \lambda & 0 & 0 & 0 & 0 \\ (1-\lambda)^2 & 2(1-\lambda)\lambda & \lambda^2 & 0 & 0 & 0 \\ 1-\lambda & 0 & 0 & \lambda & 0 & 0 \\ (1-\lambda)^2 & (1-\lambda)\lambda & 0 & (1-\lambda)\lambda & \lambda^2 & 0 \\ (1-\lambda)^2 & 0 & 0 & 2(1-\lambda)\lambda & 0 & \lambda^2 \end{pmatrix}. \quad (8)$$